PCCP

ROYAL SOCIETY OF CHEMISTRY

PAPER

View Article Online
View Journal | View Issue

Check for updates

Cite this: *Phys. Chem. Chem. Phys.*, 2026, **28**, 6853

DFT insights into metal-functionalized black phosphorene as a potential volatile organic compound sensor for early cancer detection

D. Ramkumar, K. A. Jeeva Vergin Raj, C. Preferencial Kala* and R. M. Hariharan

Received 30th December 2025,
Accepted 11th February 2026

DOI: 10.1039/d5cp05052a

rsc.li/pccp

Volatile organic compounds (VOCs) in human breath are increasingly being recognized as powerful non-invasive indicators of cancer, yet achieving their selective and real-time detection at trace levels remains a major challenge. Herein, noble metal-decorated black phosphorene (BP) is introduced as a new class of nanosensors for head and neck cancer (HNC) biomarkers. The interactions of limonene, 2,2-dimethylpropanoic acid, and 3-methylhexane with the sensing substrates were investigated using first-principles calculations based on the density functional theory (DFT) combined with the non-equilibrium Green's function (NEGF) approach. Pristine BP was found to exhibit only weak physisorption (−27.98 to −40.52 kJ mol^{-1}), whereas metal (Au, Ag, and Cu) functionalization dramatically enhanced its sensitivity. Among the systems examined, Ag@BP exhibited the strongest adsorption energy of −129.29 kJ mol^{-1} (limonene), −56.93 kJ mol^{-1} (2,2-dimethylpropanoic acid), and −36.66 kJ mol^{-1} (3-methylhexane). These interactions induced a noticeable charge rearrangement, the formation of electronic states in proximity to the Fermi energy level, and a transition from the semiconducting to metallic behaviour. Current–voltage analysis revealed remarkable sensitivity enhancements as Ag@BP achieved 90–95% conductance changes, whereas pristine BP showed only 1–65%. Recovery time calculations further highlighted the strong chemisorption of limonene (4.4×10^{10} s at 298 K, shortened to 35.8 s at 498 K) and ultrafast desorption of 2,2-dimethylpropanoic acid (6.17×10^{-4} s) and 3-methylhexane (2.65×10^{-6} s), ensuring stability with reversible operation. These findings prove that Ag@BP is a highly sensitive and recyclable 2D nanoplatform for real-time breath-based cancer diagnostics.

1. Introduction

Head and Neck Cancer (HNC) is a heterogeneous collection of cancers occurring predominantly in the oral cavity, larynx, and pharynx and ranks sixth in incidence among all cancer cases recorded worldwide.[1] HNC accounted for more than 930 000 new cases and an estimated 467 000 mortality cases in 2020 alone.[2] The pathogenesis of HNC is multi-factorial, and the most important risk factors are tobacco use, alcohol use, and infection with high-risk Human papillomavirus (HPV) types.[3] Even with the progress in surgery, radiotherapy, and immunotherapy, the five-year survival rate for HNC is still comparatively low, particularly in the patients with advanced stages of the disease.[3] Early diagnosis remains critical for maximizing the clinical outcomes; however, the current diagnostic techniques, such as endoscopy, imaging, and tissue biopsy, are invasive, expensive, and often undertaken only after symptom development.[4] Non-invasive diagnostic techniques have recently emerged as a promising alternative. In particular, breathomics focuses on the characterization of VOCs produced during human respiration.[5] It has been found that HNC patients possess specific VOC signatures in their breath, *i.e.*, higher levels of limonene, 2,2-dimethylpropanoic acid, and 3-methylhexane, among others.[6,7] These biomolecules originate from tumour tissue metabolic reprogramming, inflammation, and oxidative stress, and these biomolecules are an excellent window into the tumour disease progression and potential early screening in the future. However, the practical success of VOC-based breath diagnostics depends strongly on creating sensor platforms that offer high selectivity, high sensitivity, and long-term stability. These VOC sensors must be capable of qualitative and quantitative detection of VOCs at trace concentrations under typical ambient conditions.[8] Such breath sensors enable cheap, non-invasive sampling and real-time exhaled breath analysis and thus offer a patient-comfortable alternative to invasive conventional diagnostic techniques. Thus, VOC sensors will soon be an integral component of future medical devices to allow the early diagnosis and real-time monitoring of various pathological and physiological events in the human body.[9,10]

Centre for Materials Sciences and Nanodevices, Department of Physics and Nanotechnology, SRM Institute of Science and Technology, Kattankulathur 603203, India. E-mail: preferec@srmist.edu.in

Two-dimensional (2D) nanomaterials show huge potential for nano-sensors to detect trace levels of volatile organic compounds (VOCs) because of their high surface-area-to-volume ratio. In recent years, researchers have shown growing interest in designing biosensing conductors with different 2D nanomaterials, particularly for the purpose of breath diagnostics.[11–13] The spectacular success of graphene has prompted extensive investigation into other two-dimensional nanomaterials such as transition metal dichalcogenides (TMDs), silicene, MoS_2, borophene, MXenes, and borocarbide.[14,15] Among these, black phosphorene (BP), a single monolayer of black phosphorus, stands out as a highly promising material due to its tunable direct band gap (~0.3–2.0 eV depending on the layer number), good carrier mobility, and surface reactivity.[16,17] BP is also non-toxic and biodegradable, and thus, there is interest in biomedical devices and breath-based disease diagnosis.[18] In addition to these merits, pristine BP has a low adsorption capacity and poor sensitivity towards certain VOCs, constraining its actual application in highly sensitive sensors.[19] To overcome such weaknesses, surface functionalization is one of the strategies that has been established. In particular, metal functionalization using transition or noble metals has proven highly effective in enhancing both the sensing performance and stability of BP. Experimental and theoretical studies have consistently demonstrated that metal-decorated BP nanosheets exhibit stronger molecular interactions and more pronounced modulation of electronic properties compared to pristine BP, making them highly promising candidates for next-generation BP biomedical sensors.[20]

Previous first-principles studies have demonstrated that DFT can effectively serve as a follow-up to experimental achievements and as a powerful framework to understand bonding mechanisms and interface effects in functionalized materials. For example, Medeiros *et al.*[21] showed that metal functionalization induces significant electronic restructuring and modified interfacial bonding characteristics, which critically govern the electronic and chemical properties of low-dimensional systems. These insights provide a strong theoretical foundation for modeling metal–substrate interactions in materials of varying composition. Verma *et al.* reported a flexible hybrid sensor based on MWCNT/Nb_2O_5, which functions at room temperature and selectively detects acetone, a biomarker for diabetes, having a rapid response (25 s), rapid recovery (46 s), and low limit of detection (330 ppb), with great potential for non-invasive diagnosis.[22] Kumar *et al.* demonstrated the ultrahigh sensitivity and selectivity of the $Ti_3C_2O_2$ MXene towards Alzheimer's disease VOC biomarkers, such as BHT, with strong adsorption and excellent charge transfer. Their DFT calculation also showed induced magnetism and altered transport properties, indicating that $Ti_3C_2O_2$ is a promising material for selective breath-based biosensors.[23] In another study, Aasi *et al.* employed DFT with NEGF simulations and showed that Pt-functionalization of phosphorene improves the adsorption of alcohol, with ~41% conductance modulation for methanol/ethanol and ultrafast recovery times of 0.17 s when exposed to UV light.[24] Gilani *et al.* demonstrated that Au-decoration significantly enhances the adsorption of lung-cancer-related VOCs on WTe_2, with physisorption being dominant and ethanol exhibiting the highest sensitivity.[20] Liu *et al.* described that Al-doped $MoSe_2$ has higher adsorption and sensing capacity towards typical VOCs in exhaled breath, with the order of adsorption being $C_5H_8 > C_3H_6O > C_3H_4O$. Their work demonstrated that Al–$MoSe_2$ is highly thermostable and reversibly desorbs, making it a candidate for a resistance-type sensor for the detection of early lung cancer.[25] Panigrahi *et al.* demonstrated that $Ti_3C_2T_x$ MXenes are good adsorbents of lung cancer-associated VOCs, which cause detectable electronic property changes due to their positive adsorption energies. Based on their DFT and thermodynamic studies, they proposed $Ti_3C_2T_x$ as a potential nanosensor platform for detecting early lung cancer from exhaled breath.[26]

Meng Guo *et al.*[27] reported that first-principles calculations revealed strong and selective adsorption of CO, NH_3, NO, NO_2, and SO_2 on two-dimensional Si_9C_{15}, leading to significant band-gap modulation (0.10–1.78 eV). Among these gases, NO_2 exhibited the strongest adsorption and highest charge transfer, inducing spin-polarized semiconducting behaviour and the highest sensing sensitivity (93%). Yang Shen *et al.*[28] reported that O-defective g-ZnO exhibited enhanced VOC sensing performance, where reduced adsorption energy and charge transfer improved desorption ability and sensor reversibility. They further demonstrated the high sensitivity of the ODZO sensor toward CH_2O, C_2H_4O, and CH_4O, highlighting its potential for efficient VOC detection. Meng Guo *et al.*[29] reported that VOC adsorption on two-dimensional XC (X = Ge and Si) is strongly dependent on the adsorption configuration, and that XC-based sensors exhibit reversible sensing behaviour with rapid, temperature-assisted recovery, particularly showing high selectivity toward CH_4. Zhen Cui *et al.*[30] reported that W-vacancy-defective WS_2 exhibited markedly enhanced sensitivity and selectivity toward HCHO compared to other toxic gases. They demonstrated that HCHO adsorption induced the largest charge transfer, pronounced work-function modulation, and a great change in *I–V* characteristics, leading to the highest sensing response. On the experimental front, Li *et al.* fabricated an rGO/SnO_2-based electronic nose that was capable of sensing formaldehyde, a clinically relevant lung cancer biomarker at ppb-level concentrations.[31] Also, graphene-coated quartz crystal microbalance and surface plasmon resonance sensors exhibited sub-3 s response times with excellent sensitivity towards chlorinated and aromatic VOCs like dichloromethane, chloroform, benzene, and toluene, justifying the potential of graphene interfaces in breath diagnostics.[32]

In this study, we carried out a detailed investigation on pristine and metal (Au, Ag, and Cu)-decorated BP for detecting head and neck cancer-related VOC biomarkers using a breath-based sensing strategy. The selected biomarkers include limonene ($C_{10}H_{16}$), 2,2-dimethylpropanoic acid ($C_5H_6O_2$), and 3-methylhexane (C_7H_{16}), which are the predominant VOCs associated with HNC. In addition, CO_2 and H_2O molecules, which are commonly present in exhaled breath, were considered as potential interfering species. All the simulations in this work were performed with a DFT-NEGF combined approach to gain deep insight into the sensing behaviour. Key descriptors like adsorption energies, charge transfer, total density of states, band dispersion, recovery times, and *I–V* responses were investigated for the pristine and metal-modified BP. The results show that metal functionalization significantly enhances the sensing capability of BP, forming stronger binding interactions and improving sensitivity, desorption dynamics, and selectivity toward VOC biomarkers. These enhancements highlight metal-decorated BP as a promising platform for the non-invasive detection of head-and-neck-cancer-related VOCs.

2. Computational methods

The Quantum Atomistic Toolkit package (version 2024.09) was utilized to investigate the energetic characteristics, geometric structural arrangement, VOC adsorption performance, and electronic behaviour of the system within the framework that integrates density functional theory with the non-equilibrium Green's function (NEGF) approach.[33–35] The exchange correlation interactions were described using the Perdew–Burke–Ernzerhof (PBE) generalized gradient approximation (GGA).[36,37] To underestimating the energy band gap, the Heyd–Scuseria–Ernzerhof (HSE06) functional[38] was employed for more accurate electronic–structure and band-gap predictions. The calculations employed a linear combination of atomic orbitals (LCAO) framework, using the Fritz–Haber Institute (FHI) basis with a double-zeta plus polarization (DZP) set, which offers an accurate representation of the electronic wave functions while maintaining reasonable computational cost.[39] A Truncation Accuracy (TA) mesh cut-off energy of 90 Hartree was employed to ensure a sufficiently large plane-wave expansion for reliable total-energy calculations while keeping the computational effort manageable.[40] Long-range dispersion interactions were incorporated through the DFT-D2 correction since standard GGA-PBE fails to properly capture vdW interactions that are crucial for weak physisorption processes.[41] Geometrical optimization was performed until the residual forces and stresses were reduced below 0.01 eV Å^{-1} and 0.001 eV Å^{-1}, respectively, to guarantee that the equilibrium structures were obtained with reliable accuracy.[42] To avoid any artificial interactions arising from periodic boundary conditions, a vacuum region of 30 Å was added along the non-periodic direction of the supercell, thereby avoiding spurious interlayer coupling between periodic images.[43] Although the HSE06 functional offers superior accuracy in predicting band gaps, its improvement in describing the overall band structure and density of states (DOS) remains limited. This is evident from the minimal variations observed among different computational methods when band gap corrections are excluded, as discussed later in the text. Consequently, in this study, the HSE06 functional was used solely for accurate band gap estimation, whereas the PBE functional was adopted as the standard approach for all other electronic property analyses.[44,45]

2.1 Computational and analytical techniques

The adsorption energy (E_{ads}) was used to quantify the strength and nature of interaction between the VOC molecules and the noble metal-decorated BP surface. It was evaluated using the following expression (1):

$$E_{\text{ads}} = E_{\text{M-BP/VOCs}} - E_{\text{M-BP}} - E_{\text{VOCs}} + \text{BSSE} \tag{1}$$

where $E_{\text{M-BP/VOCs}}$, $E_{\text{M-BP}}$ and E_{VOCs} denote the total energies of the VOC adsorbed metal-decorated BP system, the isolated metal-decorated BP surface, and the free VOC molecule, respectively.[14,46,47] We have also included the basis-set superposition error (BSSE) in the calculation of adsorption energy for achieving more accuracy using the Boys–Bernardi counterpoise method.[48] Mulliken population analysis was performed to quantify the charge transfer (Q) between the target analytes and sensing system, as defined in eqn (2):

$$\Delta Q = Q_2 - Q_1 \tag{2}$$

In the target molecule, a positive ΔQ indicates that electrons are donated, whereas a negative ΔQ shows that electrons are accepted.[20,49] Another important parameter for evaluating the performance of a VOC sensing device is its sensitivity. The sensitivity (S) is defined as the relative change in the conductance of the nanosensor before and after VOC exposure, as expressed in eqn (3):

$$S = \left|\frac{G_{\text{gas}} - G_{\text{pure}}}{G_{\text{pure}}}\right| \times 100, \tag{3}$$

where G_{pure} and G_{gas} represent the conductivity of the pristine or metal-decorated BP before and after exposure to VOCs, respectively.[50–52] Moreover, the recovery behaviour of the metal-decorated BP monolayer was assessed using the van't Hoff-Arrhenius transition state theory,[53–55] as expressed in eqn (4):

$$\tau = {V_0}^{-1} \exp\left(\frac{-E_{\text{ad}}}{k_{\text{B}}T}\right), \tag{4}$$

where V_0 is the attempted frequency (taken as 10^{12} s^{-1}), E_{ad} denotes the adsorption energy, k_{B} is the Boltzmann constant (8.6173303×10^{-5} eV), and the sensor's temperature was set to 298 K. The electron transport calculation for pristine and metal-decorated BP was conducted using DFT combined with the NEGF approach. In the device setup, metal electrodes were connected to the central region along the *Z*-axis (transport direction). A 1 × 3 × 50 Monkhorst–Pack *k*-points mesh was employed to sample the Brillouin zone for the electron transport calculations.[56,57] The electrical current under an applied bias voltage (V_{b}) was computed using the Landauer–Buttiker formalism (5):

$$I = \frac{2e}{h}\int_{\mu_{\text{L}}}^{\mu_{\text{R}}} T(E, V_{\text{b}})[f_{\text{R}}(E, V_{\text{b}}) - f_{\text{L}}(E, V_{\text{b}})]\text{d}E, \tag{5}$$

where $T(E)$, $f(E)$, and E represent the transmission function, Fermi–Dirac distribution, and the electron energy, respectively. The terms μ_{L} and μ_{R} denote the chemical potentials of the left and right electrodes, respectively.

3. Results and discussion

3.1. Adsorption and electronic properties of VOCs on pristine BP

Ramkumar *et al.* previously showed through first-principles DFT and NEGF that decoration with noble metals (Au, Ag, and Cu) remarkably improves the sensing performance of black phosphorene nanosheets toward VOCs relevant to cancer diagnosis.[58] Their study revealed that the metal add-atoms substantially improve the surface reactivity of BP by strengthening molecule–substrate interactions, promoting efficient charge transfer, and including significant electronic modulations such as band gap narrowing and Fermi-level realignment. Collectively, these effects synergistically lead to superior sensitivity and selectivity toward VOC biomarkers, positioning metal-functionalized BP as a promising platform for next-generation nanoelectronic sensors.[58] Building upon these findings, the present work systematically investigates the intrinsic adsorption and electronic behaviour of pristine BP towards VOCs such as limonene, 2,2-dimethylpropanoic acid, 3-methylhexane, CO_2, and H_2O to establish a fundamental reference for its baseline sensing performance. The most energetically favourable adsorption configurations of these molecules on the BP surface were identified through complete structural relaxation, as illustrated in Fig. 1. For each adsorbate, different initial adsorption configurations were examined by placing the molecules in both horizontal and vertical orientations with respect to the BP surface, and the most stable geometry was selected based on the minimum total energy using a vdW-corrected DFT-D2 framework;[15] the corresponding energetic comparison is provided in Table S1 (SI). To elucidate the sensing mechanism, key physicochemical parameters, including adsorption energy (E_{ad}), equilibrium distance (d), charge transfer (ΔQ), recovery time (τ), and corresponding variations in the band structure and total density of states (TDOS), were comprehensively analyzed.

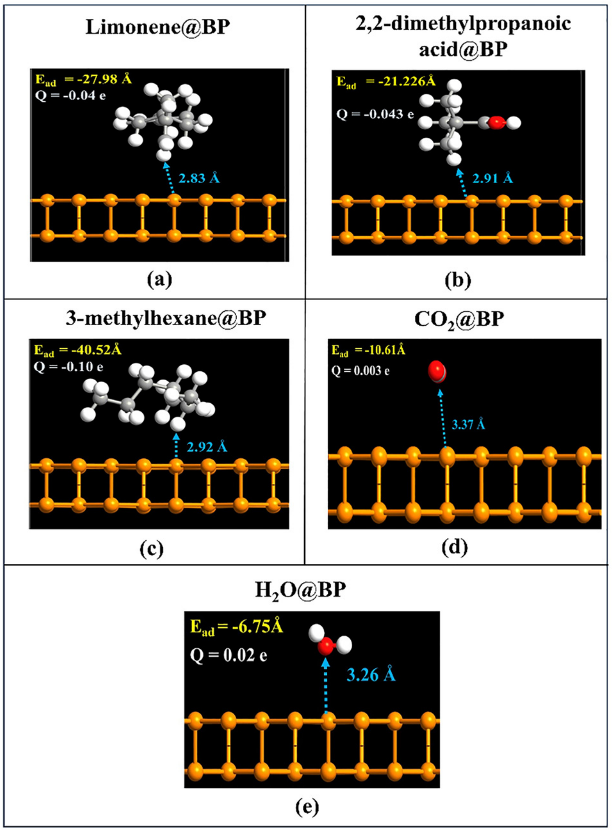

Fig. 1 Optimized configurations of VOC molecules adsorbed on pure BP: (a) limonene, (b) 2,2-dimethylpropanoic acid, (c) 3-methylhexane, (d) CO_2, and (e) H_2O.

In this context, the adsorption behaviour and electronic properties of the selected VOC biomarkers on pristine BP were systematically investigated. Upon structural optimization, all molecules were found to adsorb weakly on the BP surface in parallel orientations, stabilized primarily through van der Waals interactions, thereby confirming the physisorptive nature of binding. No lattice distortion or structural deformation was observed in BP following adsorption, highlighting its excellent mechanical and electronic robustness. The optimized adsorption distances were determined to be 2.83 Å (limonene), 2.91 Å (2,2-dimethylpropanoic acid), 2.92 Å (3-methylhexane), 3.26 Å (H_2O), and 3.37 Å (CO_2), with corresponding adsorption energies of −27.981, −21.226, −40.523, −6.754, and −10.613 kJ mol^{-1}, respectively (Table 1). These adsorption energies confirm the thermodynamically stable interactions between the VOCs and BP. The Mulliken charge transfer values $-0.04e$ (limonene), $-0.043e$ (2,2-dimethylpropanoic acid), $-0.10e$ (3-methylhexane), $+0.025e$ (H_2O), and $+0.003e$ (CO_2) indicate minimal electronic redistribution, reinforcing the dominance of non-covalent interactions.

The TDOS and band structure analyses (Fig. 2a–c) collectively reveal that VOC adsorption exerts a negligible influence on the intrinsic electronic nature of BP. As shown, the calculated TDOS for pure BP is highlighted in the blue region, exhibiting a clearly defined semiconducting profile with a band gap of ≈0.88 eV. The latter is almost preserved after molecular adsorption with an estimated value of ≈0.87 eV. The discrete molecular states (shown in green) are clearly separated from the BP states, while the corresponding TDOS of the combined systems (in dark blue) appear only with minor edge broadening without any new state formation near the Fermi level. This indicates weak orbital overlap with very minimal charge transfer between the VOCs and BP. Correspondingly, the band structures exhibit identical dispersion patterns before and after adsorption, where the band edges are well preserved without any mid-gap states, further confirming that the semiconducting integrity of BP is retained. These features collectively signify van der Waals-dominated physisorption, which is characterized by weak electronic coupling between the molecular frontier orbitals and the P-3p states of BP. Notably, (Fig. 2a–c) presents results for limonene, 2,2-dimethylpropanoic acid, and 3-methylhexane, whereas the CO_2 and H_2O analyses are provided in Fig. S1 and S2 (SI) for completeness. The electron density difference (EDD) and electron localization function (ELF) analysis (Fig. 3a–c) offer additional insight into the charge redistribution occurring at the

Table 1 Calculated interaction distance D (Å), adsorption energy (E_{ad}), band gap (E_g), charge transfer Q (e), and recovery time (τ) for each system

						T = 298 K	
System	VOCs	D (Å)	E_{ad} (kJ mol^{-1})	E_g (eV)	Q (e)	τ (s) (visible)	τ (s) (UV)
Pristine	—	—	—	—	—	—	—
	Limonene	2.83	−27.98	0.87	−0.04	7.9×10^{-8}	7.9×10^{-11}
	2,2-Dimethylpropanoic acid	2.91	−21.22	0.87	−0.043	1.2×10^{-5}	1.2×10^{-8}
	3-Methylhexane	2.92	−40.52	0.87	−0.10	5.2×10^{-9}	5.2×10^{-12}
	H_2O	3.26	−6.75	0.87	0.025	1.5×10^{-11}	1.5×10^{-14}
	CO_2	3.37	−10.61	0.88	0.003	7.2×10^{-11}	7.2×10^{-11}
Ag@BP	—	—	—	—	—	—	—
	Limonene	2.35	−129.29	0	0.087	4.4×10^{10}	4.4×10^{7}
	2,2-Dimethylpropanoic acid	2.93	−50.17	0	0.004	6.1×10^{-4}	6.1×10^{-7}
	3-Methylhexane	2.28	−36.66	0	0.037	2.6×10^{-6}	2.6×10^{-9}
	H_2O	2.44	−45.34	0	0.166	8.8×10^{-5}	8.8×10^{-8}
	CO_2	3.11	−8.68	0	0.028	3.3×10^{-11}	3.3×10^{-14}
Au@BP	—	—	—	—	—	—	—
	Limonene	2.21	−37.62	0	−0.021	3.9×10^{-6}	3.9×10^{-9}
	2,2-Dimethylpropanoic acid	2.93	−11.57	0	−0.034	1.0×10^{-10}	1.0×10^{-13}
	3-Methylhexane	2.84	−35.69	0	−0.057	1.7×10^{-6}	1.0×10^{-9}
	H_2O	2.56	−26.05	0	0.142	3.6×10^{-8}	3.6×10^{-11}
	CO_2	3.26	−7.71	0	0.001	2.2×10^{-11}	2.2×10^{-14}
Cu@BP	—	—	—	—	—	—	—
	Limonene	2.11	−77.18	0	0.164	33.40	0.03
	2,2-Dimethylpropanoic acid	2.97	−10.61	0	0.007	7.2×10^{-11}	7.2×10^{-14}
	3-Methylhexane	1.90	−56.92	0	0.038	9.4×10^{-3}	9.4×10^{-6}
	H_2O	2.16	−56.92	0	0.206	9.4×10^{-3}	9.4×10^{-6}
	CO_2	3.03	−7.71	0	0.032	2.2×10^{-11}	2.2×10^{-14}

interface. Slight charge accumulation (yellow) and depletion (black) regions were localized near the adsorption sites, with ELF values close to 0.5, typical of van der Waals interactions. No significant electron localization was observed between the molecule and substrate, further validating the physisorption mechanism. The corresponding EDD and ELF analyses for CO_2 and H_2O are provided in the SI for completeness. Kinetic analysis revealed ultrafast desorption dynamics, with recovery times of 7.9×10^{-8} s (limonene), 1.2×10^{-5} s (2,2-dimethylpropanoic acid), 5.23×10^{-9} s (3-methylhexane), 1.52×10^{-11} s (H_2O), and 7.23×10^{-11} s (CO_2) at 298 K. The combination of rapid recovery, minimal charge transfer, and unaltered electronic structure underscores that pristine BP exhibits weak yet reversible adsorption toward both VOCs and ambient molecules. Collectively, these findings identify pristine BP as an electronically stable and inert reference platform, establishing a necessary baseline for quantifying the enhancement effects introduced by noble metal decoration in BP-based VOC nanosensors.

4. Adsorption and electronic properties of VOCs on metal-decorated BP

Biomarkers were adsorbed on pristine BP weakly, and no strong sensing behaviour was observed. To overcome this limitation, noble metal atoms such as Au, Ag, and Cu were decorated onto the BP surface. Upon decoration, a strong interaction between the VOC molecules on the metal-decorated BP was noted. This was indicated by elevated adsorption energies, substantial charge transfer, and appreciable changes in the electronic structure. It was thus concluded that noble metal-decorated BP offers a better sensing platform for VOC detection than pristine BP.

4.1 Adsorption and electronic properties of limonene on Au, Ag, and Cu-decorated BP

The adsorption behaviour and electronic response of limonene on Ag@BP, Au@BP, and Cu@BP were systematically explored using optimized structures, charge redistribution maps, band-structure analysis, TDOS, EDD, and ELF, as shown in Fig. 4(a)–(l), while the corresponding adsorption parameters are summarized in Table 1. In the case of the Ag@BP system, depicted in Fig. 4(a), limonene is adsorbed in a parallel configuration with a minimum separation of 2.35 Å that yields a strong adsorption energy of −129.29 kJ mol^{-1}, which indicates chemisorption. A Mulliken charge transfer of +0.087e from limonene to Ag@BP was observed, confirming the characteristic donor–acceptor interaction in which limonene acts as the electron donor and the Ag@BP substrate serves as the electron acceptor. From the band structure analysis, it was observed that when limonene is adsorbed onto the Ag@Bp surface, the metallic character is maintained and the band gap remains at 0 eV, as shown in Fig. 4(b). This confirms that the electronic restructuring induced by Ag decoration, primarily through the hybridization of Ag 4d and P 3p orbital hybridization, remains dominant even after biomarker adsorption. The resulting Ag-induced midgap states near the Fermi level enhance charge carrier transport and electrical conductivity, enabling the sensitive detection of trace-level VOC molecules. Furthermore, the presence of flat bands near the Fermi level and the overlap between the conduction band and valence band indicate the formation of midgap states, which facilitate faster charge carrier transport and enhance the electrical

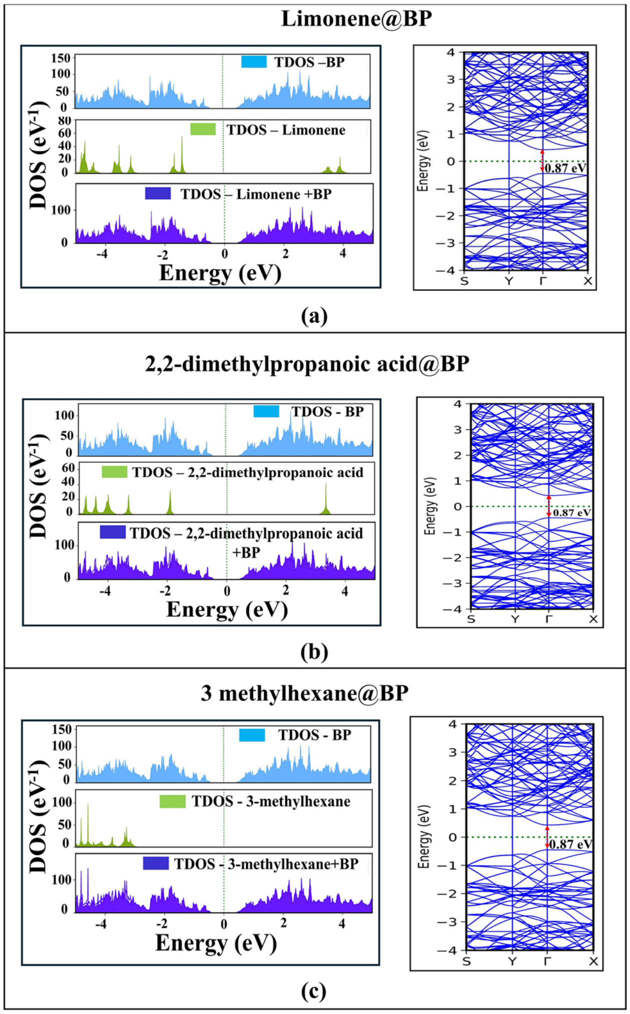

Fig. 2 TDOS and band structures of VOC molecules adsorbed on pristine BP: (a) limonene, (b) 2,2-dimethylpropanoic acid, and (c) 3-methylhexane.

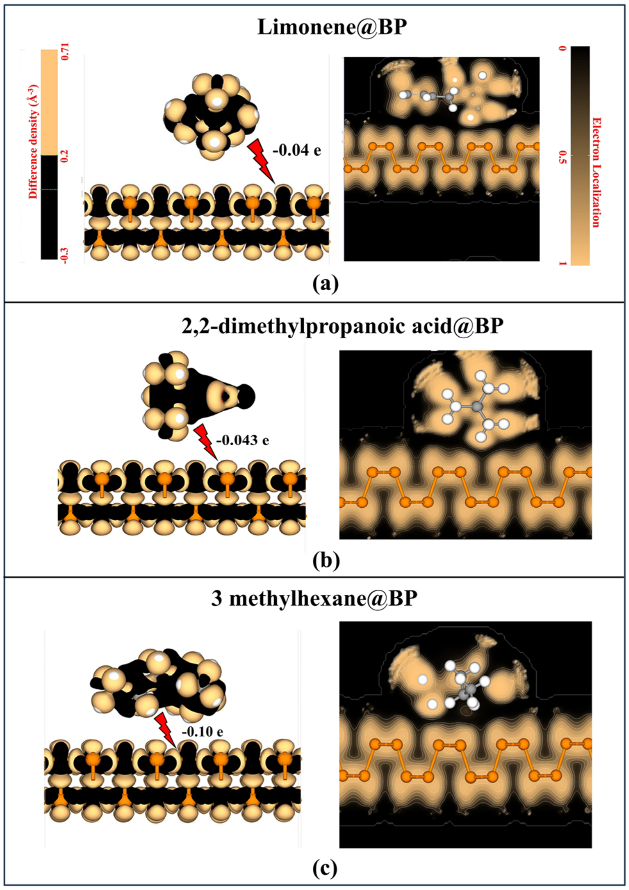

Fig. 3 EDDs and ELFs of 3 biomarkers adsorbed on pristine BP: (a) limonene, (b) 2,2-dimethylpropanoic acid, and (c) 3-methylhexane.

conductivity. Fig. 4(c) presents the total density of states of the individual components within the biomarker-adsorbed Ag@BP system. From the TDOS analysis, hydrogen (maroon colour) and carbon (pink colour) atoms in the limonene biomarker contribute localized peaks between −4 eV and 4 eV, suggesting bonding state formation. The Ag (blue colour) 4d orbitals exhibited broad peaks, indicating that they hybridized with both BP and limonene (purple colour) orbitals, supporting the strong coupling. The TDOS of the complete system demonstrated smeared states near the Fermi level, validating the electronic restructuring induced by the adsorption. The EDD and ELF maps in Fig. 4(d) show explicit electron accumulation near Ag, while depletion was observed on the biomolecule, and a partially shared electronic density between Ag-4d and P-3p states, thus confirming the weak covalent/chemisorption coupling.

In contrast, the adsorption energy of the Au@BP system Fig. 4(e) is much weaker, amounting to −37.63 kJ mol^{-1}, characteristic of physisorption. Indeed, the corresponding equilibrium separation of 2.21 Å is evidence of only a mild van der Waals contact. In terms of the band structure shown in Fig. 4(f), the system shows a zero band gap, represented by the energy band overlap at the Fermi level. The occurrence of flat bands at the Fermi level suggests the creation of localized states. This may occur when the Au 5d orbitals and the π-cloud of electrons of the limonene do not strongly interact. These mid-gap states are conduction channels allowing carriers to travel at higher speeds. The TDOS plots in Fig. 4(g) support this interpretation. A continuous non-zero TDOS is seen near the Fermi level, confirming the metallic nature of the adsorbed system. Therefore, the minimum contributions from the C (pink colour) and H (maroon colour) atoms of limonene appear in the energy range of −4 eV to 4 eV, whereas the Au 5d orbitals dominate the region near the Fermi level, suggesting that the Au atom plays an important role in modulating the electronic density near the Fermi level. The minimal charge redistribution observed in the EDD and ELF maps (Fig. 4(h)), together with the small charge transfer of −0.021e from limonene to Au@BP, corroborates a physisorption-dominated, non-covalent adsorption mechanism.

For the Cu@BP system, Fig. 4(i) shows that limonene adsorbs at a distance of 2.11 Å with an adsorption energy of −77.19 kJ mol^{-1}, positioning the interaction at the boundary between strong physisorption and weak chemisorption. The band structure of the limonene-adsorbed Cu@BP system, shown in Fig. 4(j), reveals a metallic character upon adsorption. Several flat bands emerge near

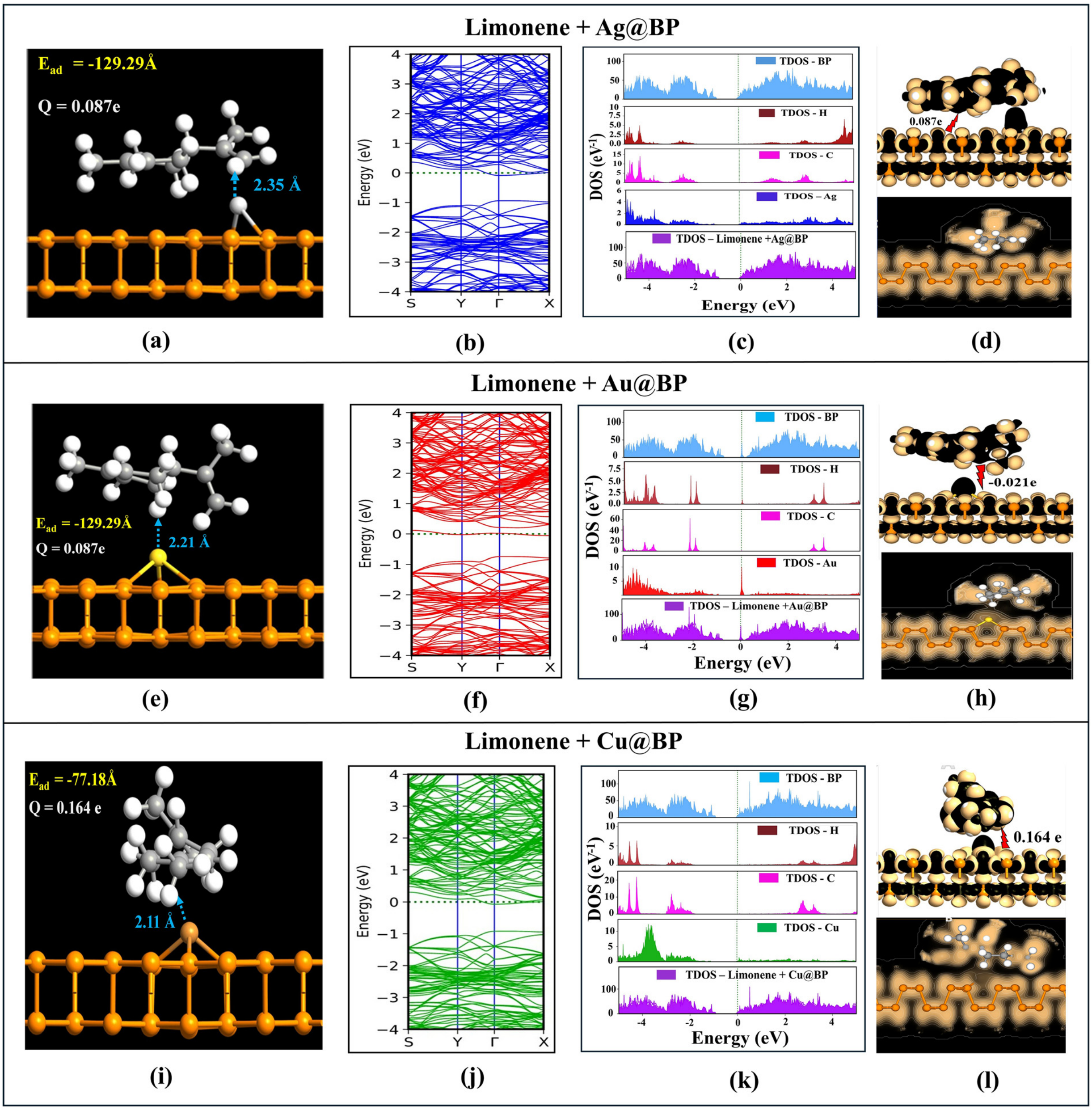

Fig. 4 Optimized adsorption geometries, band structures, total densities of states (TDOS), electron density differences (EDDs), and electron localization functions (ELFs) for limonene adsorbed on metal-decorated BPs. Panels (a)–(l) correspond to Ag@BP, Au@BP, and Cu@BP, respectively.

the Fermi level, indicative of localized electronic states introduced by the Cu-induced system. These midgap states arise from partial hybridisation between Cu 3d orbitals and the π-conjugated system of limonene. The total density of states (TDOS) shown in Fig. 4(k) supports this finding. A zero TDOS is seen at the Fermi level, confirming the system's metallic nature. The Cu 3d orbitals make the main contribution to the energy range near the Fermi level, while small peaks from the carbon and hydrogen atoms of limonene appear between −4 eV and +4 eV. The higher TDOS near the Fermi level indicates more available carriers, which could lead to greater surface reactivity and sensitivity. As evident from the EDD and ELF maps in Fig. 4(l), significant charge build-up is visible around the Cu site, and charge depletion is seen on the adsorbed molecule. These features promote a significant charge transfer of +0.164*e* from limonene to the Cu@BP substrate. The ELF demonstrated no clearly defined shared electron density between the molecule and the surface, verifying the lack of covalent bonding and thus a non-covalent character of interaction. However, the enhanced charge rearrangement indicates a strong physisorption with weak polarization effects, especially near the metal-decorated BP. Overall, the comparative analysis clearly establishes that among these limonene-adsorbed metal-decorated BP systems, Ag@BP exhibits the strongest interaction and most pronounced electronic response, followed by Cu@BP and Au@BP. This trend underlines that the choice of metal dopant critically dictates charge redistribution, interfacial electronic restructuring, and hence the sensing performance, positioning Ag@BP as the most promising platform for limonene detection. Meanwhile, Ag@BP has been successfully synthesized through both liquid-phase exfoliation, involving *in situ* Ag nanoparticle decoration on few-layer phosphorene sheets,[59] and thermal evaporation, where Ag atoms are deposited onto the BP surface to achieve controlled metal decoration and strong interfacial interaction.[60]

4.2 Adsorption and electronic properties of 2,2-dimethylpropanoic acid on Au, Ag, and Cu-decorated BP

To explore the molecular recognition characteristics of nonpolar hydrocarbons on noble-metal-modified black phosphorene (BP), the adsorption and electronic responses of 3-methylhexane on Au@BP, Ag@BP, and Cu@BP were systematically analyzed. As shown in Fig. 5(a), 2,2-dimethylpropanoic acid adsorbs on the Ag@BP surface with its carboxyl group facing the Ag site in a nearly parallel configuration. The corresponding interatomic distance of 2.93 Å and adsorption energy of −50.172 kJ mol^{-1} (Table 1) are indicative of weak van der Waals interactions, which is consistent with physisorption. In line with this weak interaction, the band structure shown in Fig. 5(b) exhibits no band gap, with the Fermi level crossing several energy states, confirming that the metallic nature of Ag@BP remains unaltered upon adsorption. The TDOS profile, seen in Fig. 5(c), does

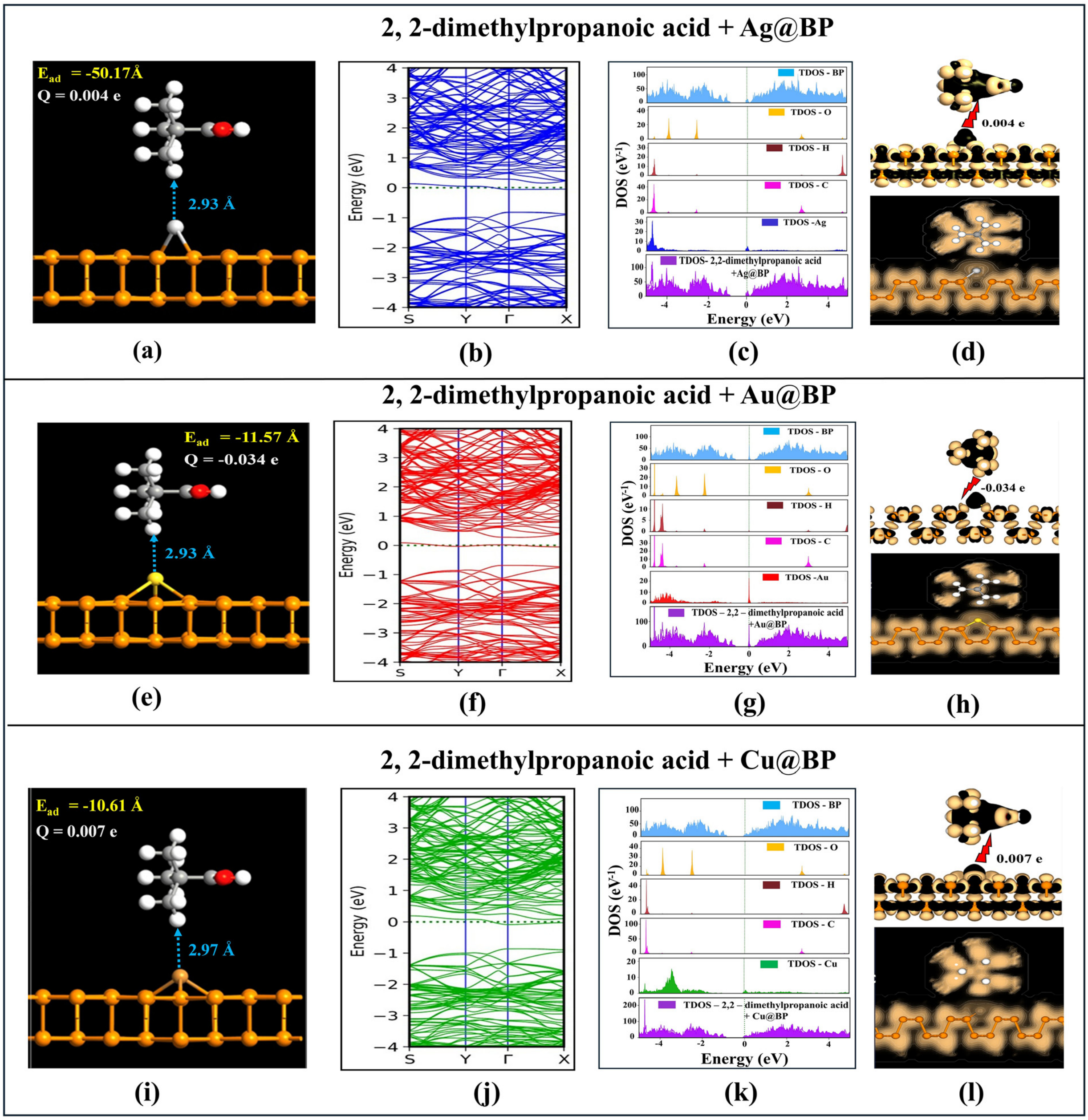

Fig. 5 Optimized adsorption geometries, band structures, total densities of states (TDOS), electron density differences (EDDs), and electron localization functions (ELFs) for 2,2-dimethylpropanoic acid adsorbed on metal-decorated BPs. Panels (a)–(l) correspond to Ag@BP, Au@BP, and Cu@BP, respectively.

not show any obvious changes after adsorption, which means Ag still dominates the electronic behaviour, while the molecular orbitals of oxygen, carbon, and hydrogen remain localized away from the Fermi level. Fig. 5(d) shows EDD and ELF maps that visually reveal the charge rearrangement confined in the immediate vicinity of the Ag atom and the hydrogen atom of the carboxyl group. One can easily observe from the EDD map a small charge accumulation around the Ag site and a slight depletion around the biomarker, which is in agreement with the rather small charge transfer of 0.004*e* from Ag@BP to the molecule. The negligible redistribution across the interface points to very weak electronic coupling between the biomarker and the substrate. Additionally, the ELF map shows that electron densities are highly localized at the individual atomic sites, particularly in the biomarker region and Ag sites, and do not share any common delocalized electron clouds. These results bear witness to the non-existence of covalent bonding, which establishes the non-covalent nature of the interaction.

Fig. 5(e) illustrates the optimised structure of 2,2-dimethylpropanoic acid adsorbed on Au@BP in a parallel configuration, where the carboxylic hydrogen atom is directed toward the Au site. The interatomic distance between the carboxylic hydrogen and the Au site is 2.93 Å. The adsorption energy was calculated as −11.578 kJ mol^{-1}, which confirmed that the interaction is largely physisorptive in nature; the 2,2-dimethylpropanoic acid molecule relaxed slightly and settled above the Au site without forming any chemical bond. The large interatomic distance confirmed a non-covalent interaction, with no structural distortion, consistent with weak van der Waals physisorption. The electronic band structure and TDOS are illustrated in Fig. 5(f) and (g). Upon adsorption of the 2,2-dimethylpropanoic acid, the metallic nature was retained. The presence of flat bands near the Fermi level in the band structure suggests that localized electronic states were formed, likely due to a weak interaction between the Au 5d orbital and the π-orbitals of the 2,2-dimethylpropanoic acid biomarker. These states remained spatially localized with very limited overlap, which is characteristic of systems where physisorption is the dominant interaction. These are also reflected in the TDOS as broad features without sharp peaks. These localized states are mainly contributed by the Au atom, as indicated by the dominant red coloured states near the Fermi level. The molecular contributions from oxygen (orange colour), carbon (pink colour), and hydrogen (maroon colour) atoms are minimal and appear in the energy range from −4 eV to 4 eV, showing poor hybridization with the substrate. The absence of significant hybridized peaks further suggests that the interaction has a physisorptive nature. Fig. 5(h) displays the EDD and ELF plots, which support the nature of adsorption. The EDD plot clearly shows that electrons were slightly depleted around the hydrogen atom and mildly accumulated near the Au atom. This confirmed a weak charge transfer of −0.034*e* from the biomarker to the Au@BP system, further indicating that the interaction is predominantly governed by van der Waals forces.

As presented in Fig. 5(i), the 2,2-dimethylpropanoic acid adsorbs on Cu@BP *via* its carboxyl group towards the Cu site, keeping the distance equal to 2.97 Å. The large adsorption distance, combined with the low adsorption energy of −10.613 kJ mol^{-1} and the negligible charge transfer of 0.007*e* (Table 1), indicates that the interaction is governed by weak van der Waals rather than covalent bonding. The band structure, shown in Fig. 5(j), remains metallic upon adsorption, although the appearance of flat bands near the Fermi level hints at localized molecular states with a relatively low degree of electronic coupling. This is further supported by the TDOS shown in Fig. 5(k), displaying sharp, well-separated peaks of O, C, and H orbitals far from the Fermi level, while states associated with Cu dominate near it. Thus, the metallic nature of the electronic properties is preserved when 2,2-dimethylpropanoic acid is adsorbed onto the Cu@BP substrate. Further confirmation was provided by the EDD and ELF maps shown in Fig. 5(l), where only a little charge redistribution was realized, and no electron sharing was found between the molecule and the substrate. These features manifest minimum orbital overlap and only a very weak donor–acceptor interaction, characteristic of physisorption. Overall, 2,2-dimethylpropanoic acid exhibited weak but stable adsorption on metal-decorated BP, preserving the substrate's metallic conductivity and structural stability. Among the three metals, Ag provides the most balanced interaction, making it well-suited for reliable and reusable VOC sensor applications.

4.3 Adsorption and electronic properties of 3-methylhexane on Au, Ag, and Cu-decorated BP

To investigate the molecular recognition properties of nonpolar hydrocarbons on noble-metal-decorated black phosphorene (BP), the adsorption and electronic responses of 3-methylhexane on Au@BP, Ag@BP, and Cu@BP were systematically investigated.

Fig. 6(a) depicts the biomarker parallel to the Ag@BP surface at a minimum distance of 2.28 Å from the Ag atom. This is a longer distance than would be typical of covalent bonds, so it suggests physisorption without bond formation. The physisorptive nature of the interaction of 3-methylhexane with Ag@BP is evident from the modest adsorption energy of −36.664 kJ mol^{-1} (Table 1) within the normal van der Waals range. Support for weak interaction comes from the small amount of charge transfer of 0.037*e* (Table 1), which shows a negligible electronic perturbation. The lack of appreciable orbital hybridization supports non-covalent binding dominated by dispersion forces over chemical bonding. The absence of significant orbital hybridization points to a non-covalent binding regime, where the interaction is mainly electrostatic and does not involve the formation of chemical bonds. Fig. 6(b) shows that the adsorption of 3-methylhexane does not alter the metallic character of Ag@BP. The conduction bands still overlapped at around the Fermi level, since physisorption is weak and there is little orbital overlap to cause a notable change in electronic structure. The TDOS of the 3-methylhexane + Ag@BP system, shown in Fig. 6(c), illustrates the elemental contributions after adsorption. The pristine BP atoms (sky blue) dominate the states near the Fermi level, preserving the metallic conduction of the substrate. The Ag atoms (dark blue) show localized 4d states primarily near the Fermi level, with minimal

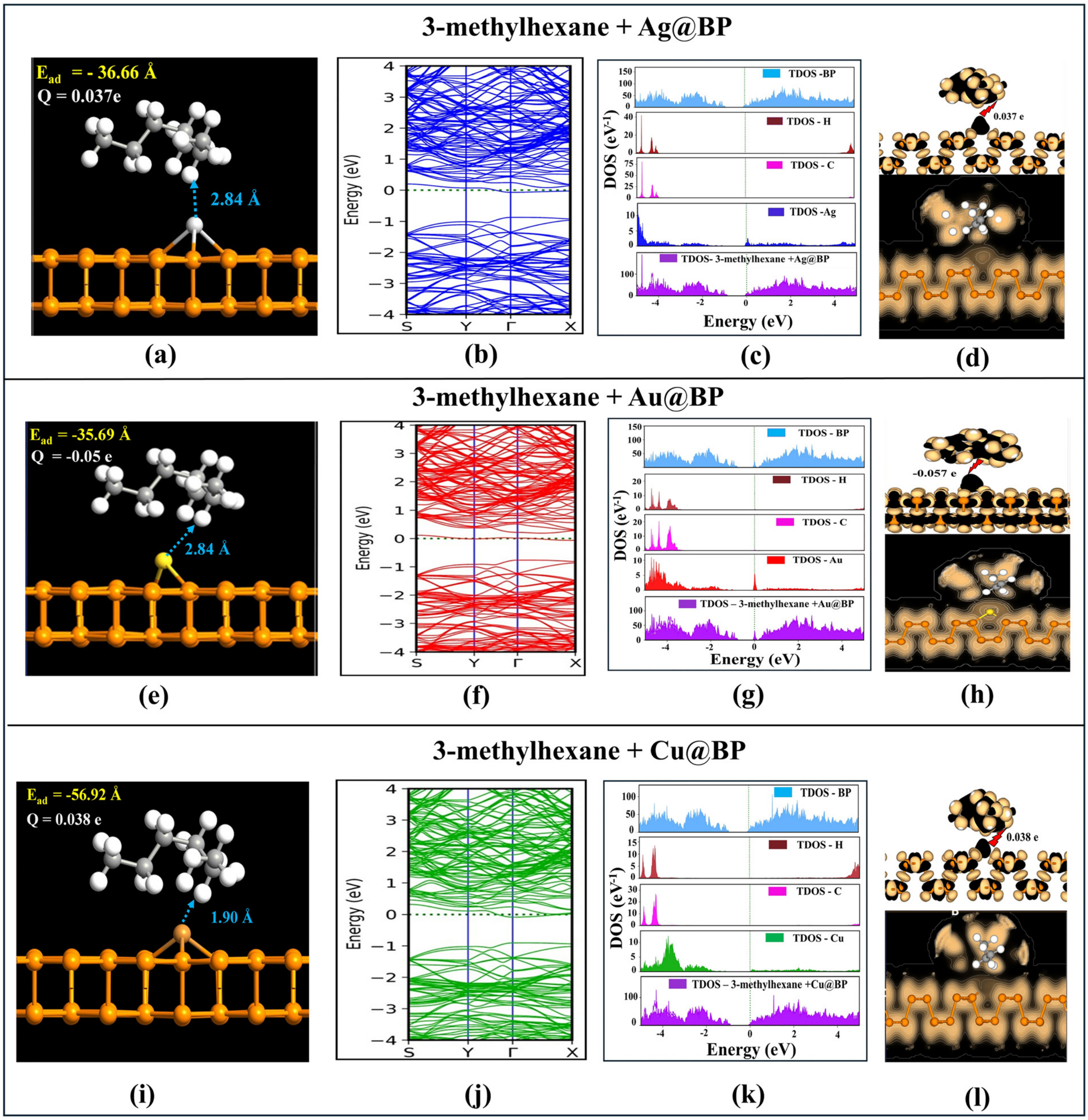

Fig. 6 Optimized adsorption geometries, band structures, total densities of states (TDOS), electron density differences (EDDs), and electron localization functions (ELFs) for 3-methylhexane adsorbed on metal-decorated BPs. Panels (a)–(l) correspond to Ag@BP, Au@BP, and Cu@BP, respectively.

hybridization with the adsorbate states. Carbon (pink) and hydrogen (brown) atoms of 3-methylhexane contribute states far away from the Fermi level, predominantly in deep valence and higher conduction regions, indicating their minor role in charge transport. The summed TDOS (purple) indicates no gap opening at the Fermi level, as for the band structure, proving that adsorption is controlled by weak van der Waals forces and not changing the metallic nature of Ag@BP. Fig. 6(d) shows that the EDD and ELF graphs collectively confirm the non-covalent interaction. The EDD graph distinctly indicates localized charge buildup close to the Ag site with minor depletion across the hydrocarbon with poor orbital overlap. Also, ELF isosurfaces indicate delocalized brownish electron clouds around the Ag atom, confirming no covalent bond formation and van der Waals forces.

Upon adsorption, 3-methylhexane assumes a nearly parallel orientation on the Au-decorated BP surface with a close Au–H distance of 2.84 Å Fig. 6(e). The moderate adsorption energy (-35.7 kJ mol^{-1}) combined with a negligible amount of charge transfer $-0.057e$ (Table 1) is indicative of weak van der Waals binding dominated by surface polarization effects. As can be seen in Fig. 6(f), the band dispersion presents metallic continuity, showing the Fermi level crossing several electronic states. Coherently, TDOS, Fig. 6(g), indicates that the electronic response is dominated by the states of Au, while the molecular orbitals of carbon and hydrogen remain localized far from the Fermi level, with very negligible hybridization. These results establish that 3-methylhexane interacts through weak surface polarization without compromising the intrinsic metallicity or structural integrity of Au@BP, an essential feature of stable, reusable molecular sensing platforms. The EDD and ELF distributions depicted in Fig. 6(h) clearly show only faint charge accumulation near the Au site and an absence of shared electronic density across the interface, indicating that this interaction is purely non-covalent.

Fig. 6(i) shows that during geometry optimization, the biomarker moves from an initial distance of 3.04 Å to a final 2.23 Å from the Cu site. This is driven by weak but cumulative van der Waals forces, balancing attraction and Pauli repulsion, resulting in a stable physisorbed state without chemical bond formation. Fig. 6(j) and (k) indicates the band structure and total density of states. The band structure of Cu@BP exhibits metallic behaviour, with the Fermi level intersecting conduction states. After the adsorption of 3-methylhexane, the overall band dispersion remains unchanged, and the overall system retains a zero-band gap. The TDOS shows the overall electronic contribution of the system. The TDOS of pristine BP atoms contributes strongly to the states near the Fermi level, dominating conductive behaviour. Cu (green colour) shows localized 3d-states contributions below the Fermi level, but no significant hybridization with adsorbate states near the Fermi level. Carbon (pink) and hydrogen (brown) from 3-methylhexane contribute states far from the Fermi level, primarily in the deep valence and high conduction regions, indicating negligible involvement in charge transport. Overall, the TDOS confirmed that adsorption occurs *via* weak physisorptive interactions, leaving the Cu@BP metallic electronic structure essentially unaltered and the band gap at zero. Fig. 6(l) depicts the EDD and ELF plots of 3-methylhexane adsorbed on Cu@BP. The EDD plot identifies the localized electron depletion and accumulation around the Cu site and biomarker atoms. In the ELF plot, brown zones represent low electron density inside 3-methylhexane, while high localization still exists around atomic centres. The lack of a continuous electron density between the biomarker and Cu@BP reinforces a non-covalent interaction. Both the EDD and ELF analyses show that the van der Waals forces are dominant in maintaining the inherent electronic structure of Cu@BP. Overall, 3-methylhexane interacts only weakly with Ag@BP, Au@BP, and Cu@BP through physisorption, which results in very negligible charge transfer without significant modification of their metallic electronic structures. This suggests that nonpolar hydrocarbons induce minimal perturbation across all three decorated BP systems, thus rendering them all equally stable but only weakly responsive toward this VOC.

4.4 Adsorption and electronic properties of CO_2 on metal-decorated (Ag, Au, and Cu) BP

Fig. 7 presents the optimized structures, band structures, TDOS, EDD, and ELF maps of CO_2 on Ag@BP (a)–(d), Au@BP (e)–(h), and Cu@BP (i)–(l), with all adsorption parameters summarized in Table 1.

As shown in Fig. 7(a), the CO_2 molecule interacts weakly with the Ag@BP surface, as reflected by its adsorption distance of 3.11 Å and adsorption energy of -8.68 kJ mol^{-1}. In line with expectations, this is a very weak interaction and thus corresponds to physisorption, mainly caused by dispersion-driven van der Waals forces. In connection with this, after adsorption, the Ag@BP system remains metallic because the energy bands still cross the Fermi level, as shown in Fig. 7(b). In connection with this, after adsorption, the Ag@BP system remains metallic because the energy bands still cross the Fermi level. The Ag–P conduction network is not disturbed by the small perturbation exerted by CO_2, and new hybridized states are not created; hence, the metallic conductivity is preserved. Fig. 7(c) shows that in the TDOS, only slight peak changes in the 2–4 eV region are observed; the contributions of oxygen (orange), carbon (pink), and Ag (blue) remain well separated, which indicates that orbital overlap between CO_2 and Ag@BP is almost negligible and the overall electronic structure remains unchanged. In Fig. 7(d), the EDD and ELF plots further confirm the weak interaction. A small charge accumulation near the Ag atom with a very slight depletion on CO_2 corresponds to a minimal charge transfer of 0.028*e* from CO_2 to the Ag@BP surface. The ELF does not show any localization of electron density between CO_2 and the substrate, which confirms that the adsorption is purely non-covalent and mostly dominated by van der Waals forces. Therefore, the adsorption of CO_2 causes no change in the electronic and structural properties of Ag@BP.

The CO_2 molecule interacts weakly with the Au@BP surface, as shown in Fig. 7(e), with a calculated equilibrium separation of 3.26 Å and an adsorption energy of -7.72 kJ mol^{-1}, indicating a physisorption regime dominated by van der Waals interactions. Fig. 7(f) shows that after CO_2 adsorption, the metallic nature of the Au@BP system remains unchanged, with the band structure displaying continuous states crossing the Fermi level. Only minor electronic modulation arises from the weak interaction with CO_2, without the formation of hybridized states, which allows the delocalized Au–P conduction framework to remain unaffected. Correspondingly, the TDOS (Fig. 7(g)) has only slight changes in the peak position in the 2–4 eV range; the contributions of oxygen (orange), carbon (pink), and Au (red) remain well separated without showing any overlapping features. This points to minor orbital overlap and confirms that CO_2 adsorption has little influence on the intrinsic electronic structure of Au@BP. Accordingly, as derived from EDD and ELF analyses Fig. 7(h), faint charge accumulation is apparent near the Au site with almost negligible depletion of charge on the CO_2 molecule. This minimal charge redistribution is consistent with the extremely small charge transfer of 0.001*e* from CO_2 to the Au@BP surface, confirming a non-covalent, van der Waals-dominated interaction. More importantly, the ELF map does not indicate shared electron density between the molecule and substrate, reiterating that the adsorption is purely physisorptive and electronically inert.

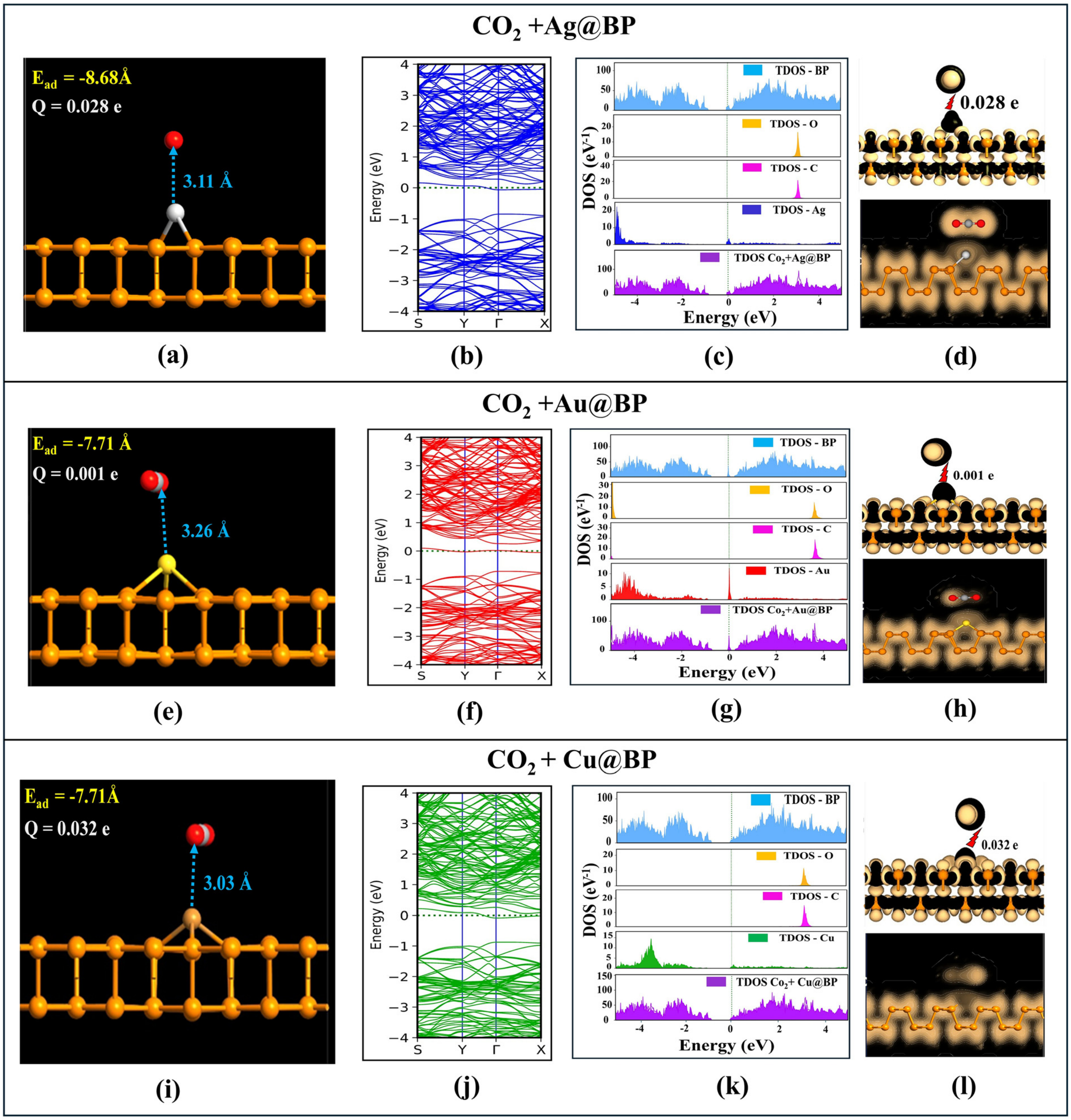

Fig. 7 Structural and electronic responses of metal-decorated black phosphorenes (BPs) upon CO_2 adsorption. Panels (a)–(d) show the optimized configurations, band structures, TDOS, and charge redistributions (EDD/ELF) for Ag@BP; and (e)–(l) depict the corresponding results for Au@BP and Cu@BP, respectively.

As illustrated in Fig. 7(i), the CO_2 molecule is physisorbed onto the Cu-decorated BP surface with an equilibrium adsorption distance of 3.03 Å and an adsorption energy of -7.72 kJ mol^{-1}, which indicates a physisorption mechanism due to van der Waals interactions. Correspondingly, the band structure in Fig. 7(j) shows that the Cu@BP system retains its intrinsic metallic nature, where several conduction bands continuously cross the Fermi level without any gap opening or band distortion. This further ascertains that CO_2 adsorption leads to minimal perturbation of the intrinsic electronic states of the Cu@BP system. The TDOS plot Fig. 7(k) indicates only subtle changes within the energy range from 2 to 3 eV, where the contributions from oxygen (orange), carbon (pink), and Cu (green) remain separate without orbital overlap. This separation means that no evident hybridization between the molecular orbitals of CO_2 and the Cu@BP substrate occurred, which further confirms the weak interaction. Moreover, Fig. 7(l) shows that a slightly enhanced charge accumulation is located around the site of Cu with a very small charge transfer from CO_2 to Cu@BP of 0.032*e*, corresponding to very minor charge depletion around the CO_2 molecule, as shown by EDD and ELF maps. The absence of localized electron density between CO_2 and the surface from the ELF map again confirms that this interaction is purely non-covalent and electronically inert, allowing Cu@BP to maintain stability and conductivity upon CO_2 adsorption.

4.5 Adsorption and electronic properties of H_2O on metal-decorated (Ag, Au, and Cu) BP

As indicated by Fig. 8(a), the H_2O molecule is weakly physisorbed on the Ag@BP surface at an adsorption distance of 2.97 Å with an adsorption energy of −10.48 kJ mol^{-1}, as listed in Table 1. The interaction is dominated by van der Waals forces with negligible orbital hybridization. The band structure indicated in Fig. 8(b) confirms that the metallic nature of Ag@BP remains unchanged after H_2O adsorption since its electronic bands keep crossing the Fermi level without any noticeable distortion. In the TDOS plot of Fig. 8(c), only minor changes were observed between 1–3 eV, with the orbital contributions of oxygen (orange), hydrogen (maroon), and Ag (blue) remaining well separated. This separation confirms that H_2O adsorption does not significantly alter the near-Fermi electronic states. Fig. 8(d) shows that EDD and ELF plots are associated with faint charge accumulation near the Ag atom and slight depletion around the H_2O molecule, corresponding to a very minimal charge transfer of 0.025*e*. The absence of any shared electron density in the ELF profile confirms that the

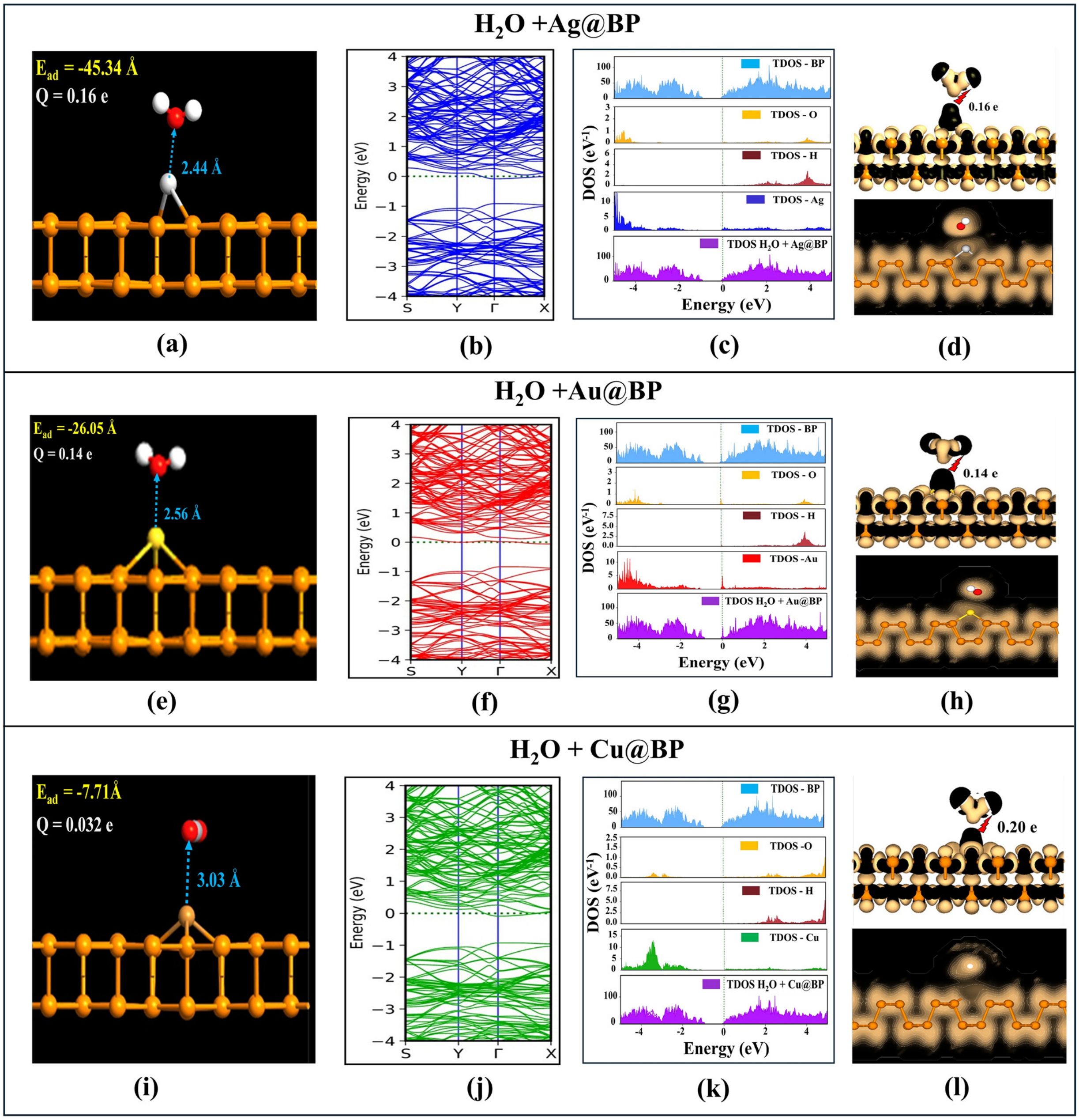

Fig. 8 Optimized adsorption geometries, band structures, total densities of states (TDOS), and charge redistribution profiles (EDD and ELF) for H_2O adsorbed on metal-decorated black phosphorene (BP). Panels (a)–(l) correspond to Ag@BP, Au@BP, and Cu@BP, respectively.

interaction is non-covalent in nature and of physisorptive character, leaving Ag@BP structurally and electronically intact.

As shown in Fig. 8(e), the H_2O molecule is only weakly adsorbed above the Au site with an equilibrium distance of 3.02 Å and an adsorption energy of -9.21 kJ mol^{-1}, indicating a dispersion-dominated physisorption regime. The band structure plotted in Fig. 8f shows continuous metallic bands crossing the Fermi level, which indicates that the intrinsic metallicity of Au@BP is unaffected by the adsorption of H_2O. The TDOS spectra in Fig. 8(g) indicate only minor peak modulations within the energy range of 2–4 eV. In particular, the contributions of oxygen (orange), hydrogen (maroon), and Au (red) remain distinct, with no orbital overlap between these contributions. These are indicative of negligible hybridization between H_2O and the Au@BP surface. Indeed, the corresponding EDD and ELF maps in Fig. 8(h) illustrate weak charge accumulation localized around the Au atom and a minor depletion around H_2O, consistent with an already determined minimal charge transfer of 0.011*e*. A key point is that no localized electron density between the two species has been found, thus proving that the interaction is purely non-covalent, without perturbing either the metallic conduction or chemical stability of Au@BP.

As shown in Fig. 8(i), the H_2O molecule is weakly adsorbed on the Cu@BP surface with an equilibrium separation of 2.88 Å and an adsorption energy of -11.25 kJ mol^{-1}, meeting the physisorption criteria. The band structure, as shown in Fig. 8(j), maintains the characteristic metallic continuity since multiple conduction bands cross the Fermi level, indicating that the electronic nature of Cu@BP is stable after adsorption. The TDOS profile Fig. 8(k) reflects slight changes within the 1–3 eV region, without any significant mixing of the orbitals from oxygen (orange), hydrogen (maroon), and Cu (green). This separation indicates the weak molecule–surface coupling. Further, the EDD and ELF plots in Fig. 8(l) illustrate small charge accumulation in the vicinity of the Cu site with its corresponding depletion around the H_2O molecule, amounting to a charge transfer of 0.029*e*. No electron localization between H_2O and the Cu@BP surface confirmed that the nature of adsorption is non-covalent and electronically inert. Therefore, this implies preservation of the metallic character and the sensing reliability of Cu@BP, even under humid conditions.

Overall, we observed that metal-decorated BP with VOCs exhibits metallic behaviour, which indicates high electrical conductivity due to the charge carrier redistribution around the Fermi level. Experimentally, the sensing response is commonly evaluated by monitoring the variation in electrical resistance or conductance as a function of analyte concentration, enabling detection down to the ppb level. Seba S. Varghese *et al.*[61] reported that charge-transfer-driven sensing behaviour is a common feature of highly conductive graphene materials, where electrical resistance can enable ppb-level detection. For instance, graphene-based sensors have demonstrated measurable conductance modulation at analyte concentrations as low as 52 ppb, arising from adsorption-induced charge transfer. Meanwhile, the metal-decorated BP metallic electronic structure provides a highly sensitive transduction platform, allowing weak VOC adsorption in clinical breath samples to be detected at ppb levels.

5. VOC sensing interpretation

5.1 Recovery time

The recovery time (τ) is considered an important factor for evaluating VOC sensor performance as it shows how quickly VOC biomarkers are released from the sensing surface after detection. A shorter τ is taken as an indication of better reversibility, which is more important for reliable, repeatable sensing. Herein, the desorption behaviours of pristine BP and metal-decorated BP (Ag@BP, Au@BP, and Cu@BP) towards VOCs have been studied at various temperatures, 298 K, 398 K, and 498 K, and the results are given in Table S2 (SI). The recovery characteristics of the studied VOCs on pristine and metal-decorated BP were evaluated at 298 K, and the results demonstrate a clear dependence on both the VOC identity and the surface modification. For pristine BP, limonene desorbs almost instantaneously with a recovery time of 7.9×10^{-8} s, whereas 2,2-dimethylpropanoic acid exhibits a comparatively slower response ($\tau = 1.2 \times 10^{-5}$ s) due to its stronger binding affinity; 3-methylhexane shows intermediate behaviour ($\tau = 5.23 \times 10^{-9}$ s). Functionalization with Ag significantly strengthens adsorption, particularly for limonene, which shows an exceedingly long $\tau = 4.4 \times 10^{10}$ s, indicating quasi-irreversible chemisorption at room temperature. In contrast, 2,2-dimethylpropanoic acid ($\tau = 6.17 \times 10^{-4}$ s) and 3-methylhexane ($\tau = 2.65 \times 10^{-6}$ s) exhibit much shorter recovery times, reflecting faster desorption and reasonable reversibility. For Au@BP, all VOCs display rapid recovery at 298 K, with τ values of 3.91×10^{-6} s (limonene), 1.0×10^{-10} s (2,2-dimethylpropanoic acid), and 1.7×10^{-6} s (3-methylhexane), confirming weak physisorption and excellent room-temperature recyclability. In the case of Cu@BP, limonene shows a moderately long $\tau = 33.40$ s, while 2,2-dimethylpropanoic acid ($\tau = 7.23 \times 10^{-11}$ s) and 3-methylhexane ($\tau = 9.41 \times 10^{-3}$ s) desorb much more readily. The thermal stability of Ag@BP has already been validated by *ab initio* molecular dynamics (AIMD) simulations in our previous work.[58] The AIMD simulation confirmed stable fluctuation without abrupt peaks and dips. This suggests that Ag@BP maintains thermal equilibrium. The potential energy fluctuation confirms the absence of phase transformation or structural degradation. Collectively, these results reveal that Au@BP supports efficient room-temperature sensing, Ag@BP exhibits strong VOC binding with limited reversibility, and Cu@BP presents a mixed desorption response depending on the VOC species.

Although black phosphorene is known to be sensitive to oxidation under ambient conditions, its structural integrity can be well preserved under controlled environments such as vacuum or inert atmospheres. The elevated temperature of 498 K employed in this work represents short-term thermal activation used to accelerate the desorption of strongly adsorbed molecules rather than continuous high-temperature operation. In practical sensor devices, encapsulation and surface passivation strategies can be applied to effectively suppress oxidation and improve the thermal durability of BP-based materials.[62,63] Therefore, the use of elevated temperatures to achieve faster recovery does not hinder the practical feasibility of black phosphorene-based sensing platforms.

5.2 *I–V* characteristics of VOC biomarkers on pristine and metal-decorated black phosphorene devices

Fig. 9 presents the *I–V* characteristics of pristine BPNS and the Ag, Au, and Cu-decorated BP devices. Among these systems, Ag@BPNS shows the strongest interaction with all examined

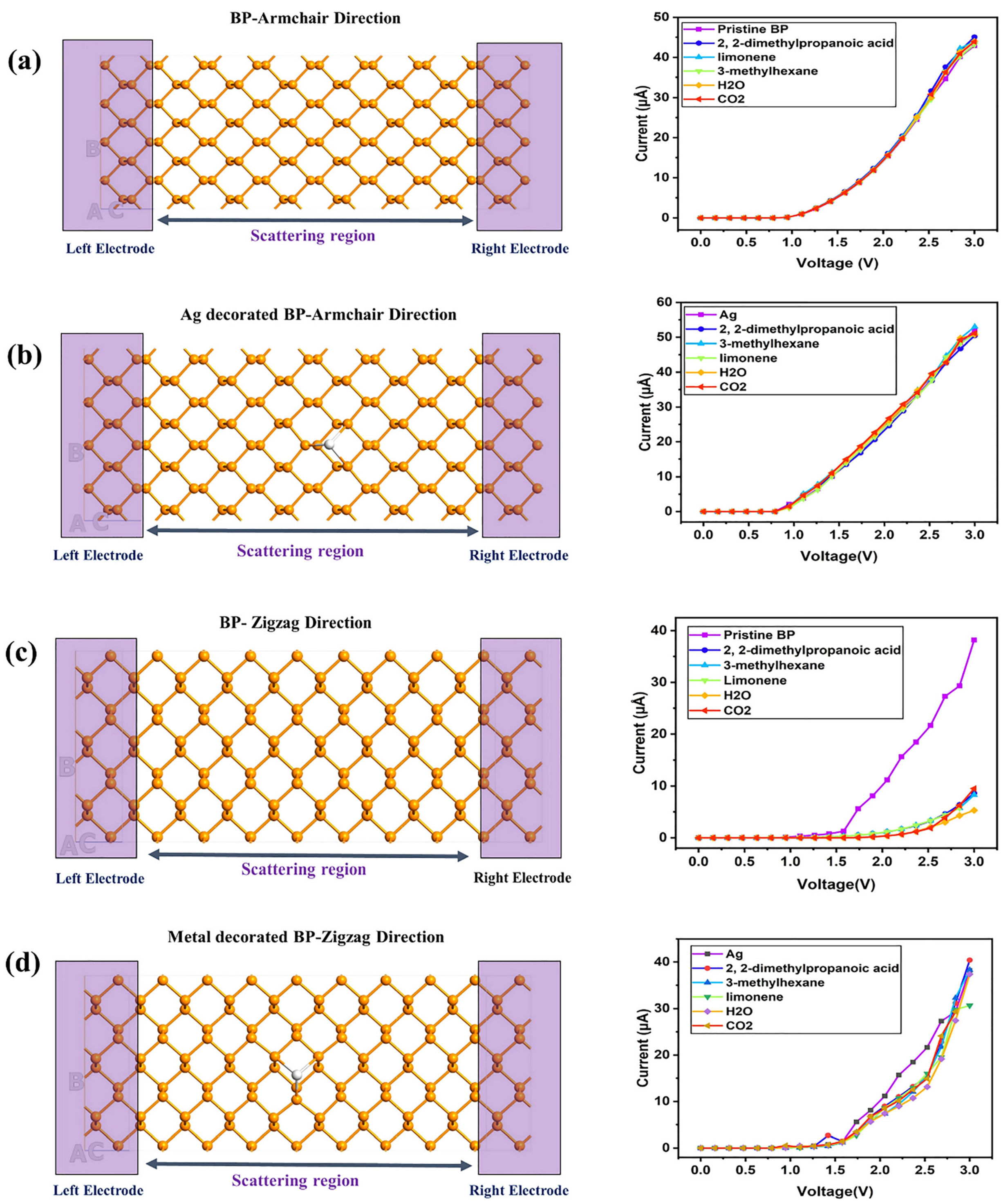

Fig. 9 Schematic of the transport model and current–voltage (*I–V*) characteristics of BPs along the two crystalline directions: (a) pristine BP in the armchair direction, (b) Ag-decorated BP in the armchair direction, (c) pristine BP in the zigzag direction, and (d) Ag-decorated BP in the zigzag direction.

biomarkers, limonene, 2,2-dimethylpropanoic acid, and 3-methylhexane, so its *I*–*V* behaviour is discussed in detail for each molecule. Conversely, Au@BPNS and Cu@BPNS showed very good adsorption only with limonene; hence, the *I*–*V* behaviour was studied for limonene adsorption for these systems. In the device setup, the left and right electrodes are periodic in the *Z*-direction (transport axis) and are joined with the centre scattering region. The left and right electrodes extend over 3.32 Å, while the scattering region spans 26.56 Å. Upon applying a bias voltage, the Fermi level of the left electrode shifts upward relative to that of the right electrode. Current begins to flow only when the valence-band maximum (VBM) of the left electrode aligns with or enters the energy range of the conduction-band minimum (CBM) of the right electrode. Once the applied bias exceeds this threshold, electron transport is activated through the device, leading to a measurable current.

From Fig. 9, the *I*–*V* conductance of the various device configurations was first obtained. Subsequently, the sensitivities of pristine BP and Ag@BP in both the armchair and zigzag transport directions were evaluated at bias voltages of 0.9, 1.5, 2.0, 2.2, and 3.0 V. Fig. 10(a) and (b) compares the sensitivity of pristine BP and Ag@BP in the armchair direction at 0.9 V, and in the zigzag direction at 2.2 V. At 0.9 V in the armchair direction, the sensitivities of 5.2% (2,2-dimethylpropanoic acid), 3.9% (limonene), and 1.2% (3-methylhexane) were recorded on pristine BP. At the same voltage, the sensitivities of 90% (2,2-dimethylpropanoic acid), 90% (limonene), and 85% (3-methylhexane) were observed on Ag@BP. Similarly, at 2.2 V in the zigzag direction (Fig. 10b), sensitivities of 65, 64 and 64% were recorded for 2,2-dimethylpropanoic acid, limonene, and 3-methylhexane on pristine BP, respectively. At the same voltage, sensitivities of 95%, 94%, and 93% were observed on Ag@BP, respectively. Selectivity was also examined by calculating the ratios of the sensitivities of 2,2-dimethylpropanoic acid relative to common interfering gases (3-methylhexane, limonene, H_2O, and CO_2) in both directions in Fig. 10(b) and (c).

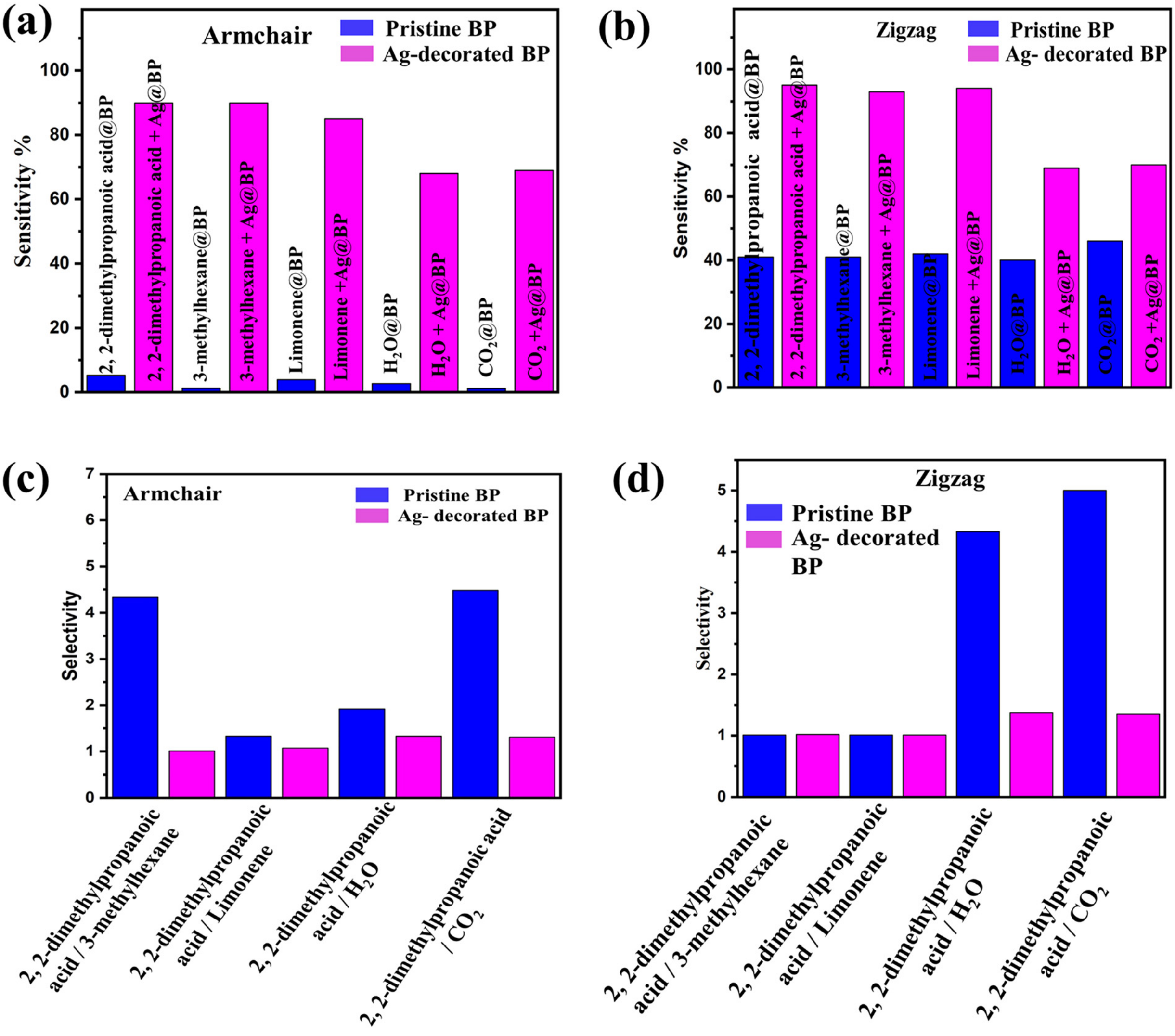

Fig. 10 Sensitivity of the VOC biomarkers adsorbed on pristine BP and Ag@BP along the (a) armchair and (b) zigzag directions. Panels (c) and (d) present the corresponding selectivity profiles.

Table 2 Comparison of the sensing performances of metal-decorated black phosphorene towards different target molecules

Metal-decorated black phosphorene	VOC biomarkers	Adsorption energy range (kJ mol^{-1})	Sensitivity (%)	Ref.
Ag-decorated black phosphorene	Limonene, 2,2-dimethylpropanoic acid, and 3-methylhexane	−21.22 to −129.29	95	This work
Pd-decorated black phosphorene	Acetone, ethanol, methanol, and toluene	−43.41 to −147.62	15.1	64
Pt-decorated black phosphorene	Acetone, ethanol, formaldehyde, methanol, and toluene	−46.31 to −158.24	41.10	24
Ag-decorated black phosphorene	NO_2	—	39.9	65

In the armchair direction, pristine BP displayed selectivity ratios of 4.33, 1.33, 1.92, and 4.48, respectively, whereas Ag@BP showed corresponding ratios of 1.01, 1.07, 1.33, and 1.31. In the zigzag direction, the selectivity ratios for pristine BP were 1.01, 1.01, 4.33, and 5.00, while Ag@BP exhibited ratios of 1.02, 1.01, 1.37, and 1.35. These results clearly indicate that although Ag functionalization significantly enhances the overall sensor response, while pristine BP exhibits slightly higher selectivity, Ag@BP offers a substantially stronger overall sensing response, making it the more effective platform for detecting 2,2-dimethylpropanoic acid.

Table 2 presents a comparison of the sensing performances of black phosphorene decorated with various metals towards different target molecules. Previous studies have sought ways of improving the sensor response of black phosphorene by introducing metals such as Ag, Pd, and Pt. In contrast, our resultsindicate that the Ag@BP device exhibits a very high sensitivity of 95%, which is higher than the previously reported values. As listed in Table 2, this high sensitivity suggests that Ag@BP is one of the most promising platforms for effective VOC biomarker detection.

6. Conclusion

Herein, the adsorption characteristics of the critical head and neck cancer (HNC) biomarkers, limonene, 2,2-dimethylpropanoic acid, and 3-methylhexane, and typical interfering gases (H_2O and CO_2) have been studied systematically on pristine and noble metal-decorated BP nanosheets through first-principles DFT calculations and the NEGF method. Pristine BP showed weak physisorption (−27.98 to −40.52 kJ mol^{-1}), which restricted its sensing capability, while metal decoration remarkably improved sensitivity. Among the functionalized systems, Ag@BP showed the highest adsorption (−129.29 kJ mol^{-1} for limonene, −56.93 kJ mol^{-1} for 2,2-dimethylpropanoic acid, and −36.66 kJ mol^{-1} for 3-methylhexane), together with charge redistribution, novel electronic states at the Fermi level, and semiconductor-to-metal transition. Current–voltage measurements clearly demonstrated the superior sensing response of Ag@BP, which exhibited conductance variations reaching 90–95%, in sharp contrast to the lower 1–65% range characteristic of pristine BP. Recovery time analysis further confirmed the rapid desorption for 2,2-dimethylpropanoic acid (6.1×10^{-4} s) and 3-methylhexane (2.6×10^{-6} s) at 298 K, demonstrating the excellent reversibility and reusability of the Ag@BP sensor. Hence, noble metal-decorated BP, especially Ag@BP, appears to be a highly sensitive, selective, and recyclable 2D nanosensor with great promise towards non-invasive, real-time breath-based cancer diagnosis.

Author contributions

All authors of this manuscript contributed to this research study. D. Ramkumar: conceptualization, data curation, and writing – original draft. K. A. Jeeva Vergin Raj: data curation, formal analysis, and visualization. C. Preferencial Kala: visualization, supervision, writing-review and editing. R. M. Hariharan: visualization, formal analysis, and data curation.

Conflicts of interest

The authors declare that they have no known competing financial interests or personal relationships that could have appeared to influence the work reported in this paper.

Data availability

The data that support the research findings of this study are not publicly available due to confidentiality of the information, data protection, and privacy, and they can be provided upon reasonable request through the proper channel.

The supplementary information (SI) includes additional data on electronic properties, adsorption analysis, and tables summarizing dispersion times. See DOI: https://doi.org/10.1039/d5cp05052a.

Acknowledgements

The authors gratefully acknowledge the financial support for this work by the DST-FIST, Government of India (Ref. no. SR/FST/PSI-155/2010). The authors convey their special thanks to the High-Performance Computing Center, SRMIST, for providing the computational facility and to all their beloved teammates.

References

1 M. Abusamak, A. Abu-Samak, W. Cai, H. Al-Waeli, F. S. Al-Hamed, M. Al-Tamimi, M. Juweid, A. Chaurasia, B. Nicolau and F. Tamimi, *Int. J. Cancer*, 2025, **156**, 1015–1032.

2 M. Leenders, S. Chuang, C. C. Dahm, K. Overvad, P. M. Ueland, Ø. Midttun, S. E. Vollset, A. Tjønneland, J. Halkjær, M. Jenab, F. Clavel-Chapelon, M. Boutron-Ruault, R. Kaaks, F. Canzian, H. Boeing, C. Weikert, A. Trichopoulou, C. Bamia, A. Naska, D. Palli, V. Pala, A. Mattiello, R. Tumino, C. Sacerdote, F. J. B. Van Duijnhoven, P. H. M. Peeters, C. H. Van Gils, E. Lund, L. Rodriguez, E. J. Duell, M. S. Pérez, E. Molina-Montes, J. M. H. Castaño, A. Barricarte, N. Larrañaga, D. Johansen, B. Lindkvist, M. Sund, W. Ye, K. Khaw, N. J. Wareham, D. S. Michaud, E. Riboli, W. W. Xun, N. E. Allen, F. L. Crowe, H. B. Bueno-de-Mesquita and P. Vineis, *Int. J. Cancer*, 2012, **131**, 997–1002.

3 L. Q. M. Chow, *N. Engl. J. Med.*, 2020, **382**, 60–72.

4 L. J. Oh, K. Phan, S. W. Kim, T. H. Low, R. Gupta and J. R. Clark, *Oral Oncol.*, 2020, **105**, 104661.

5 V. B. T. Phung, T. N. Tran, Q. H. Tran, T. T. Luong and V. A. Dinh, *ACS Omega*, 2024, **9**, 2302–2313.

6 X. Sun, K. Shao and T. Wang, *Anal. Bioanal. Chem.*, 2016, **408**, 2759–2780.

7 P. C. Moura, M. Raposo and V. Vassilenko, *Biomed. J.*, 2023, **46**, 100623.

8 P. Haripriya, M. Rangarajan and H. J. Pandya, *J. Breath Res.*, 2023, **17**, 024001.

9 R. Purkhart, H. Köhler, E. Liebler-Tenorio, M. Meyer, G. Becher, A. Kikowatz and P. Reinhold, *J. Breath Res.*, 2011, **5**, 027103.

10 F. Monedeiro, R. B. Dos Reis, F. M. Peria, C. T. G. Sares and B. S. De Martinis, *J. Breath Res.*, 2020, **14**, 026009.

11 N. Queralto, A. N. Berliner, B. Goldsmith, R. Martino, P. Rhodes and S. H. Lim, *J. Breath Res.*, 2014, **8**, 027112.

12 Y. Y. Broza and H. Haick, *Nanomedicine*, 2013, **8**, 785–806.

13 S. Saha and Md. K. Alam, *arXiv*, 2025, preprint, arXiv: 2502.17302, DOI: 10.48550/ARXIV.2502.17302.

14 Y. Yu and C. Dai, *Phys. E*, 2021, **125**, 114409.

15 A. Aasi, S. Mehdi Aghaei and B. Panchapakesan, *ACS Omega*, 2021, **6**, 4696–4707.

16 R. Majidi and M. Nadafan, *Phys. Lett. A*, 2020, **384**, 126036.

17 R. K. Mishra, J. Sarkar, I. Chianella, S. Goel and H. Y. Nezhad, *Next Materials*, 2024, **4**, 100217.

18 B. Salmankurt and H. H. Gürel, *Bull. Mater. Sci.*, 2025, **48**, 26.

19 X. Jia, H. Zhang, Z. Zhang and L. An, *Mater. Chem. Phys.*, 2020, **249**, 123114.

20 R. Gilani, S. S. Alarfaji, K. Nadeem, A. Saeed and M. Isa Khan, *RSC Adv.*, 2024, **14**, 26788–26800.

21 P. V. C. Medeiros, G. K. Gueorguiev and S. Stafström, *Phys. Rev. B: Condens. Matter Mater. Phys.*, 2012, **85**, 205423.

22 G. Verma, S. Sarraf, A. K. Basu, P. Ranjan and A. Gupta, *J. Mater. Chem. B*, 2025, **13**, 3460–3470.

23 N. Kumar, H. Bae, H. Lee, T. Hussain, A. Anand, C. V. Singh and N. Tit, *ACS Appl. Nano Mater.*, 2024, **7**, 6873–6884.

24 A. Aasi, S. M. Aghaei and B. Panchapakesan, *J. Mater. Chem. C*, 2021, **9**, 9242–9250.

25 T. Liu, Z. Cui, X. Li, H. Cui and Y. Liu, *ACS Omega*, 2021, **6**, 988–995.

26 P. Panigrahi, H. Vovusha, Y. Pal, H. Bae, H. Lee, T. Kaewmaraya, S. Nazir, M. J. A. Shiddiky and T. Hussain, *ACS Appl. Nano Mater.*, 2023, **6**, 22117–22127.

27 M. Guo, T. Zhao and Z. Cui, *Mater. Sci. Semicond. Process.*, 2026, **205**, 110352.

28 Y. Shen, P. Yuan, Z. Yuan, Z. Cui, D. Ma, F. Cheng, K. Qin, H. Wang and E. Li, *Langmuir*, 2024, **40**, 17396–17404.

29 M. Guo, T. Zhao and Z. Cui, *Surf. Interfaces*, 2024, **51**, 104607.

30 Z. Cui, H. Wang, K. Yang, Y. Shen, K. Qin, P. Yuan and E. Li, *Sensors*, 2024, **24**, 762.

31 Y. Liu, J. Li, W. Hou, Q. Zhou and W. Zeng, *J. Mater. Res. Technol.*, 2022, **18**, 4236–4247.

32 J. Song, R. Li, R. Yu, Q. Zhu, C. Li, W. He and J. Liu, *Microchem. J.*, 2024, **199**, 110051.

33 J. Taylor, H. Guo and J. Wang, *Phys. Rev. B: Condens. Matter Mater. Phys.*, 2001, **63**, 245407.

34 M. Brandbyge, J.-L. Mozos, P. Ordejón, J. Taylor and K. Stokbro, *Phys. Rev. B: Condens. Matter Mater. Phys.*, 2002, **65**, 165401.

35 J. P. Perdew, K. Burke and Y. Wang, *Phys. Rev. B: Condens. Matter Mater. Phys.*, 1996, **54**, 16533–16539.

36 H. Cui, X. Zhang, D. Chen and J. Tang, *Appl. Surf. Sci.*, 2018, **447**, 594–598.

37 S. Grimme, *J. Comput. Chem.*, 2006, **27**, 1787–1799.

38 J. Heyd and G. E. Scuseria, *J. Chem. Phys.*, 2004, **121**, 1187–1192.

39 A. Aasi, S. M. Aghaei and B. Panchapakesan, *J. Mater. Chem. C*, 2021, **9**, 9242–9250.

40 P. Srivastava, K. P. S. S. Hembram, H. Mizuseki, K.-R. Lee, S. S. Han and S. Kim, *J. Phys. Chem. C*, 2015, **119**, 6530–6538.

41 J. Princy Maria, R. Bhuvaneswari, V. Nagarajan and R. Chandiramouli, *Mol. Phys.*, 2020, **118**, e1737744.

42 J. Princy Maria, R. Bhuvaneswari, V. Nagarajan and R. Chandiramouli, *Chem. Phys. Lett.*, 2021, **771**, 138472.

43 A. Aasi, S. Mehdi Aghaei and B. Panchapakesan, *ACS Omega*, 2021, **6**, 4696–4707.

44 A. Rabiei Baboukani, S. M. Aghaei, I. Khakpour, V. Drozd, A. Aasi and C. Wang, *Surf. Sci.*, 2022, **720**, 122052.

45 M. Mahmoudi Gahrouei, N. Vlastos, R. D'Souza, E. C. Odogwu and L. De Sousa Oliveira, *J. Chem. Theory Comput.*, 2024, **20**, 3976–3992.

46 A. Bano, J. Krishna, D. K. Pandey and N. K. Gaur, *Phys. Chem. Chem. Phys.*, 2019, **21**, 4633–4640.

47 P. Karki, B. Chettri, P. Chettri, S. Kr Das and B. Sharma, *Microsyst. Technol.*, 2025, **31**, 1075–1087.

48 B. Swetha, V. Nagarajan, A. Soltani and R. Chandiramouli, *Comput. Theor. Chem.*, 2020, **1185**, 112876.

49 B. Chettri, A. Sharma, S. K. Das and B. Sharma, *Mater. Today: Proc.*, 2022, **58**, 696–701.

50 P. Lakhera, S. Singh, R. Mehla, V. Chaudhary, P. Kumar and S. Kumar, *IEEE Sensors J.*, 2022, **22**, 7572–7579.

51 J. Wu, Z. Li, A. Luo and X. Xing, *Sensors*, 2023, **23**, 7319.

52 R. P. Reji, S. K. C. Balaji, Y. Sivalingam, Y. Kawazoe and S. Velappa Jayaraman, *ACS Appl. Nano Mater.*, 2023, **6**, 5345–5356.

53 T. Wang, D. Wang, K. Xie, P. Wang, X. Li, C. Xue, L. Lin and Y. Shen, *Surf. Interfaces*, 2024, **52**, 104878.

54 V. Nagarajan and R. Chandiramouli, *Comput. Theor. Chem.*, 2021, **1203**, 113347.

55 Y.-H. Zhang, Y.-B. Chen, K.-G. Zhou, C.-H. Liu, J. Zeng, H.-L. Zhang and Y. Peng, *Nanotechnology*, 2009, **20**, 185504.

56 Y. Meir and N. S. Wingreen, *Phys. Rev. Lett.*, 1992, **68**, 2512–2515.

57 S. Singh, A. D. Sarkar and I. Kaur, *Int. J. Environ. Anal. Chem.*, 2021, **101**, 1616–1634.

58 D. Ramkumar, K. A. Jeeva Vergin Raj, C. Kala and R. Hariharan, *Surf. Interfaces*, 2025, **76**, 107944.

59 Z. Hu, Q. Li, B. Lei, J. Wu, Q. Zhou, C. Gu, X. Wen, J. Wang, Y. Liu, S. Li, Y. Zheng, J. Lu, J. He, L. Wang, Q. Xiong, J. Wang and W. Chen, *Adv. Mater.*, 2018, **30**, 1801931.

60 Y. Wang, Y. Zhou, J. Li, R. Zhang, H. Zhao and Y. Wang, *J. Hazard. Mater.*, 2022, **435**, 129086.

61 S. S. Varghese, S. Lonkar, K. K. Singh, S. Swaminathan and A. Abdala, *Sens. Actuators, B*, 2015, **218**, 160–183.

62 A. Favron, E. Gaufrès, F. Fossard, A.-L. Phaneuf-L'Heureux, N. Y.-W. Tang, P. L. Lévesque, A. Loiseau, R. Leonelli, S. Francoeur and R. Martel, *Nat. Mater.*, 2015, **14**, 826–832.

63 J. Pei, X. Gai, J. Yang, X. Wang, Z. Yu, D.-Y. Choi, B. Luther-Davies and Y. Lu, *Nat. Commun.*, 2016, **7**, 10450.

64 A. Aasi, S. M. Aghaei, S. E. Bajgani and B. Panchapakesan, *Adv. Theory Sims*, 2021, **4**, 2100256.

65 Y. Wang, Y. Zhou, J. Li, R. Zhang, H. Zhao and Y. Wang, *J. Hazard. Mater.*, 2022, **435**, 129086.